International Journal of Multiphase Flow 149 (2022) 103974

Contents lists available at ScienceDirect

International Journal of Multiphase Flow

journal homepage: www.elsevier.com/locate/ijmulflow

# Air bubble entrapment during drop impact on solid and liquid surfaces

Subhayan Halder, Rafael Granda, Jingwei Wu, Abhilash Sankaran, Vitaliy Yurkiv, Alexander L. Yarin, Farzad Mashayek *

*Department of Mechanical and Industrial Engineering, University of Illinois at Chicago, Chicago, IL 60607, USA*

ARTICLE INFO

*Keywords:*
Cahn-Hilliard-Navier-Stokes modeling
Phase-field model
Drop impact
Air bubble

ABSTRACT

The phase-field modeling (PFM) of water drop impact onto a dielectric hydrophobic parafilm surface is performed to explore air entrapment and its influence on deposition and rebound phenomena. Local and global characteristics of the drop impact are taken into account by using the combined Cahn-Hilliard and Navier-Stokes equations. The modeling results of water drop impact are directly compared with our experimental measurements in terms of maximum spreading distance, and air bubble size. The simulation results reveal that air can be trapped under the liquid drop during the initial impact as well as during the retraction phase at the center of the drop due to the closure of the liquid layer above a cavity. It is found that the drop diameter and the impact velocity play significant roles in the air entrapment phenomena. The probability of air bubble formation is higher at lower impact velocity and for larger drop size. The model is also capable of simulating the case of drop impact onto a water surface, and the results are validated using prior literature data. In addition, the influence of the phase-field variables and the mesh adaptation scheme on the PFM is studied and discussed. Thus, our findings provide new qualitative and quantitative insights into the influence of air entrapment on drop deposition onto hydrophobic and liquid surfaces.

## 1. Introduction

One of the fundamental requirements of painting and coating technologies is uniform and homogeneous deposition over the solid surface for high-quality and durable applications. However, occasional air entrapment under the liquid layer could negatively influence the durability of painting and coating layers leading to damaged solid surfaces. An extensive research on this topic has led to a better understanding of various natural phenomenon such as, impact of rain drops on water bodies or plant leaves, soil erosion by rain, and different industrial applications such as, liquid spray cooling and coating, painting, ink-jet printing, atomization (Jian et al., 2018; Langley et al., 2018; Yarin, 2006; Yarin and Weiss, 1995), etc. However, the understanding of the influence of the entrapped air on the drop deposition at the fundamental microscale level is scarce. Thus, in the present work, a phase-field model (PFM) that enables the incorporation of microscopic details of air entrapment under the water drop at different conditions is developed and applied to simulate drop deposition onto dielectric hydrophobic surface.

The behavior of the drop after impact depends on impact velocity, size and shape as well as the properties such as surface tension, viscosity (Zhang et al., 2016), etc. The spreading and rebounding of the drop also depend on the wettability of the solid surface (Zhang et al., 2016). The surrounding gas also plays an important role in the drop impact dynamics (Mehdi-Nejad et al., 2003). One of the interesting phenomenon during drop impact is the formation of air bubble, which is highly dependent on the drop size and the impact velocity (Hung et al., 2013; Sankaran et al., 2021).

In the last few years, a large number of experiments has been conducted on drop impact on both solid and liquid surfaces. A detailed discussion of various numerical and experimental work regarding liquid drops impact is provided by Yarin (2006) and Yarin et al. (2017). Rioboo et al. (2002) study quantitively the influence of different parameters such as drop diameter, drop velocity, liquid surface tension and viscosity, surface roughness and wettability on the outcome of drop impact onto a solid surface. Moita and Moreira, 2002 demonstrate that surface roughness plays an important role for a range of Reynolds number (*Re*) and Weber number (*We*). When impacting on a solid surface which is super-hydrophobic in nature the water drop can fully bounce back (Richard and Quéré, 2000). Xu et al. (2005) showed that the surrounding gas can have a great effect on the shape and spreading of the drop during impact.

* Corresponding author.
*E-mail address:* mashayek@uic.edu (F. Mashayek).

https://doi.org/10.1016/j.ijmultiphaseflow.2022.103974
Received 26 June 2021; Received in revised form 10 December 2021; Accepted 10 January 2022
Available online 12 January 2022

The entrapment of air bubble inside the liquid drop during impact has gained a lot of attention in the early 1990s. Chandra and Avedisian (1991) have first shown the formation of small air bubble inside the drop during the impact of n-heptane liquid drops on steel plate surface. Air entrapment during drop impact on liquid surfaces is also reported in literature (Elmore, 1990; Hasan and Prosperetti, 1990). Weiss and Yarin (1999) performed numerical simulation of drop impact onto liquid films using boundary-integral method and analyzed the effect of the impact Weber number on crown formation and entrapment of air bubble. Two different kinds of bubble entrapment during drop impact on solid surfaces have been previously reported in the literature. The first one is called *impact bubble* which is formed during the spreading due to the enclosure of thin air layer under the drop (van Dam and Le Clerc, 2004). Such a bubble entrapment could also stem from the electric forces affecting the prompt splashing during drop splashing (Sankaran et al., 2021). Bouwhuis et al. (2012) have conducted both experiments and numerical simulations using boundary-integral method to analyze the entrapment of air bubble formed during the initial impact of the ethanol drop on solid surfaces. For ethanol drop impacting on a smooth glass surface they demonstrated that there exists an optimum point based on the drop size and impact velocity, where the volume of the entrapped bubble is maximum. The second type is called *entrapped bubble* which is formed during the retraction of the drop when the liquid layer of the drop encloses above an air cavity (Ford and Furmidge, 1967; Hung et al., 2013; Wang et al., 2012; Wu et al., 2021).

It is challenging to study experimentally the effect of characteristic parameters and variables on air bubble formation. Alternatively, numerical simulations allow exploring a large parameter space with different variables and non-dimensional numbers to reveal the mechanistic details of the origin of air entrapment phenomenon. Various methods have been developed to model drop impact onto surfaces (Wörner, 2012), all of which can be mainly classified into two groups, atomistic models and mesoscale models. Among the mesoscale models, the level set method (Akhlaghi Amiri and Hamouda, 2013; Caviezel et al., 2008), the volume of fluid method (Huang et al., 2012; Yokoi et al., 2009), the spine-flux method (Mashayek and Ashgriz, 1995a, 1995b), the lattice Boltzmann method (Huang et al., 2012; Mitchell et al., 2018; Tanaka et al., 2011) and the phase-field model (Jacqmin, 2000, 1999; Prokopev et al., 2019; Song et al., 2019; Vorobev et al., 2020; Vorobev and Lyubimova, 2019; Wang et al., 2016; Yurkiv et al., 2018) are more commonly used.

The phase-field modeling method or PFM, more specifically referred to as the coupled Cahn-Hilliard-Navier-Stokes (CHNS) in the context of the present problem, is one of the most highly regarded methods to model a two-phase flow either liquid-air or liquid-liquid. For modeling of drop impacts, the PFM helps to account for the topological changes of the liquid drop shape with more ease. The basic concept and derivation of the governing equations regarding PFM is described by Jacqmin (2000, 1999) in details. Precisely, Jacqmin shows how to bind the solutions of the Cahn-Hilliard (CH) equation and the Navier-Stokes (NS) equations, by adding the continuum force into the NS equation and by consideration of the velocity field obtained from the solution of the NS equation into the modified CH equation. Several models have been later developed using PFM for simulation of two-phase flow. (Bai et al., 2017) perform a study of the drop formation process in a flow focusing on a micro-channel at a low capillary number. They investigate the effect of the size, the velocity along the downstream and the period of formation of the drop and compare experimental and numerical results both qualitatively anf quantitavely. An independent approach ideologically close to the standard CHNS was developed in Yarin et al. (2005a, 2005b) and applied to modeling of evaporation and precipitation of liquid blobs inside carbon nanotubes. Zhang et al. (2016) apply the CHNS model and study numerically the spreading, splashing and rebounding phenomena during drop impact and investigate the effects of the Reynolds number and the Weber Number. Yurkiv et al. (2018) implement the CHNS modeling for the simulation of liquid drop impact onto a solid dielectric surface. They explain the effect of the applied voltage on the spreading, rebounding of the drop and perform a comparative analysis between the numerical and experimental observations. Lyubimova et al. (2019) investigated the evolution of an isothermal binary mixture of two miscible liquids in a confined domain. They reported that the interface thickness is inversely proportional to the surface tension. Wörner et al. (2021) developed a diffuse interface phase-field solver to study the spreading and rebound dynamics of sub-millimeter urea-water-solution on hydrophobic substrates.

In this work, the PFM method is used to predict air bubble formation in case of water drop impact on parafilm surface. Parafilm is a flexible semi-transparent film which is hydrophobic. The static contact angle of water drops on the parafilm surface is taken from the experimental measurements as $103^0$. Two-dimensional axisymmetric domain is used for all calculaitons. Several cases varying drop size and impact velocity are considered. The relation between the drop size and impact velocity using the dimensionless numbers (i.e., *We* and *Fr*) is discussed. The modeling results are compared to our own experimental measurements in terms of the maximum spreading distance of the drop on the solid surface. Additionally, the PFM is applied to simulate the formation of entrapped air bubble during water drop impact on water surface and the results are compared with prior literature (Hasan and Prosperetti, 1990; Pumphrey and Walton, 1988).

The structure of the present paper is as follows: First, the experimental and numerical methodologies are described. Then, the results of water drop impact on both parafilm surface (solid) and water (liquid) are presented. At the end, conclusions are presented considering both numerical and experimental results.

## 2. Methodology

### 2.1. Experimental

The experimental setup is similar to our previous work (Sankaran et al., 2021; Yurkiv et al., 2021). Two types of experiments have been conducted. In the first type, drops of different sizes (diameters) are released onto a parafilm substrate from a fixed height. Parafilm M Laboratory Film was obtained from Bemis manufacturer (#PM992). The drop evolution upon their impact in the middle of the substrate is recorded. In the second type of experiments, drops of a fixed size are dripped onto the parafilm substrate from different heights (variable impact velocities), and the resulting drop impact dynamics is investigated.

Parafilm is overlaid on a glass slide and used as a dielectric substrate for drop impact. Each specimen is carefully cut as a 2 cm (length) $\times$ 2 cm (width) piece. The glass slide with the parafilm substrate on top of it is mounted on an adjustable platform, which could be adjusted in three directions. In particular, the height between the tip of the needle, which releases drops, and the substrate surface can be adjusted. Additionally, a fine-tune control along one of the horizontal axes allows one to aim the center of the substrate for drop impact. In the case of experiments of the first type, a needle height of $h = 11.5$ cm is fixed and the average impact velocity is 1.45 $\mathrm{m{\cdot}s^{-1}}$(measured from the video recordings). This velocity is slightly lower (due to the effect of the air drag) than the estimate of $\sqrt{2gh} = 1.50\ \mathrm{m{\cdot}s^{-1}}$, with g being the gravitational acceleration.

Pure water is used as the working fluid in all the experiments. A laboratory syringe pump (NE-1000 Series) supplies the liquid into the 90°- bent 30G (G stands for gauge), 27G, 25G and 21G stainless steel dispensing needles obtained from McMASTER-CARR, at the flow rate of 4 mL/h, which allows one to vary drop sizes. The out-of-focus 90° bent needles facilitates placing the top camera right above the needles to visualize the top view during drop impact and spreading. The average drop diameters are about 2.20 mm, 2.50 mm, 2.65 mm and 3.07 mm when the 30G, 27G, 25G and 21G needles are used, respectively.

In the experiments of the second type, water is supplied at a flow rate

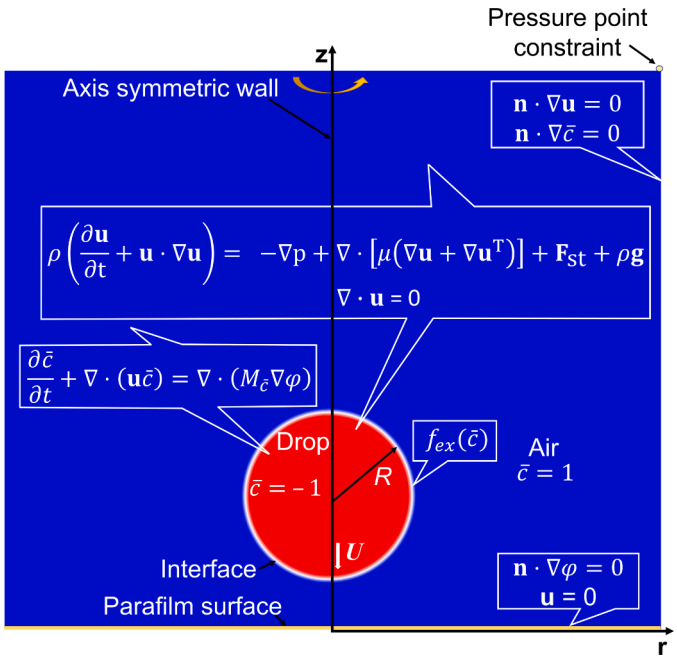


**Fig. 1.** Sketch of the computational domain, main governing equations and the necessary boundary conditions used. The domain initially occupied by liquid is shown in red, the domain initially occupied by air is shown in blue. The parafilm surface is shown in yellow color at the bottom (For interpretation of the references to color in this figure legend, the reader is referred to the web version of this article).

of 4 mL/h to a 90° bent 27G needle. The average drop diameter is about 2.50 mm. Here, drops detach and fall, due to gravity, onto the parafilm substrate from different heights, and hence, variable impact velocities are controlled by the height of the needle over the substrate. Only normal drop impacts are studied here.

In order to simultaneously visualize the side and top views during drop impact and evolution, two high-speed cameras (Phantom V210 and Phantom Miro 4) are set up and synchronized. For the side viewing, back lighting (LED lamp) illuminates the drop, and for the top viewing, front lighting is employed. In recording the side views, the center of the lens of the camera is aligned at the same horizontal level as that of the parafilm substrate. The impact velocity is determined by the drop motion observed in the side view. All measurements and experiments are performed at room temperature.

### 2.2. Numerical

The simulation domain is defined in a 2-D axisymmetric cylindrical coordinate system, where drop impact is assumed to take place normally onto the solid surface that is considered to be ideally smooth (negligible surface roughness). Fig. 1 illustrates the computational domain, the main governing equations and the boundary conditions required for the simulation.

The fundamental concepts of the described model is based upon the work of Jacqmin (2000, 1999) and Yurkiv et al. (2018). The modeling domain consists of two phases, the liquid drop (water) and the surrounding air (gas). The main difference between PFM and other interface tracking methods (Mashayek and Ashgriz, 1995a, 1995b) is that in PFM a finite interface thickness between the two fluids is considered whereas most other methods consider a sharp interface (Levich, 1962; Wörner, 2012). In addition to that, the PFM method facilitates a thermodynamic treatment of the phase interfaces, which makes it more physically consistent for simulations of two-phase flows (Lowengrub and Truskinovsky, 1998).

In the PFM, the free energy functional $(F(c))$ is considered as the summation of different types of energy existing in the system (Jacqmin, 1999; Yurkiv et al., 2018)

$$F(\bar{c})=\int_{V}[f_{ch}(\bar{c})+f_{ex}(\bar{c})]\mathrm{d}V. \tag{1}$$

In Eq. (1), the term $f_{ch}(\bar{c})$ defines the chemical free energy density which is a function of the phase-field variable $\bar{c}$. This variable is used to model the two phases, with $\bar{c}=1$ for the surrounding air phase and $\bar{c}=-1$ for the liquid water drop phase. $f_{ex}(\bar{c})$ denotes the excess free energy due to the inhomogeneous distribution of the volume fraction $(\bar{c})$ in the interface region. The expressions for $f_{ch}(\bar{c})$ and $f_{ex}(\bar{c})$ are given in Yurkiv et al. (2018). The Cahn-Hilliard equation combined with the advective term, which is a result of the minimization of the free energy, is used to express the evolution of the phase-field variable $\bar{c}$ (Jacqmin, 1999),

$$\frac{\partial\bar{c}}{\partial t}+\nabla\cdot(\mathbf{u}\bar{c})=\nabla\cdot(M_{\bar{c}}\nabla\varphi) \tag{2}$$

where, $\varphi=\frac{\partial F(\bar{c})}{\partial\bar{c}}$ is the chemical potential. The fluid velocity vector $\mathbf{u}$ (all boldfaced symbols refer to vectors) in the above equation is calculated from the NS equation and thus the equations are coupled.

The phase-field equation is coupled to a fluid flow (i.e., NS) equation at the drop-air interface by means of the Two-Phase Flow, Phase Field Coupling Feature (COMSOL®, 2018). An improved conservation of the integral of the phase field variable $(\bar{c})$ is obtained using the nonconservative form provided that the discretization order of the phase field variable is equal to or lower than the order of the pressure. Thus, the best way is to use the non-conservative form initially and reduce the percentage of mass loss and then implement the conservative form.

The term $M_{\bar{c}}$ in Eq. (2) is called the phase-field mobility or the phenomenological mobility (Abels et al., 2012). This parameter determines the interface relaxation time and the timescale of diffusion in the CH equation. There are different ways to calculate the mobility. For simulations of drop impact, $M_{\bar{c}}$ is typically considered to be proportional to the square of the interface thickness (Bai et al., 2017; Lim and Lam, 2014) and can be defined as follows,

$$M_{\bar{c}}=\chi\varepsilon_{\bar{c}}^{2} \tag{3}$$

The variable $\chi$ is referred to as the mobility tuning parameter and term $\varepsilon_{\bar{c}}$ is the measurement of the interfacial thickness.

Yue et al. (2007) presented a detailed analysis of the mass loss which occurs due to the finite thickness of the interface in the PFM. By properly adjusting $\mathring{a}_{\bar{c}}$, drop mass loss can be reduced during the time of interest. In the case of drop impact onto a solid surface, the impact velocity of the drop also plays an important role along with the interface thickness, as it will change the advective term $(\nabla\cdot(\mathbf{u}\bar{c}))$ and the phase field term $(\nabla\cdot(M_{\bar{c}}\nabla\varphi))$ in the CH equation. Higher impact velocities will accelerate the mass loss (Zhang et al., 2016).

For the simulation of the two-phase fluid flow, the NS equations are used and are coupled with the CH equation (Eq. (2)). The mass balance (continuity) equation and the momentum equation are given, respectively, as follows:

$$\nabla\cdot\mathbf{u}=0 \tag{4}$$

$$\rho\left(\frac{\partial\mathbf{u}}{\partial t}+\mathbf{u}\cdot\nabla\mathbf{u}\right)=-\nabla p+\nabla\cdot\left[\mu\left(\nabla\mathbf{u}+\nabla\mathbf{u}^{T}\right)\right]+\mathbf{F}_{st}+\rho\mathbf{g} \tag{5}$$

where, $p$ is the pressure, $\rho$ is the density of the fluid, $\mu$ is the dynamic viscosity and $\mathbf{g}$ is the gravitational acceleration. The source term, $\mathbf{F}_{st}$, is the surface tension force and is used to couple the NS and the CH equations (Jacqmin, 1999),

$$\mathbf{F}_{st}=\varphi\nabla\bar{c} \tag{6}$$

This surface tension force term arises from the compositional gradient at

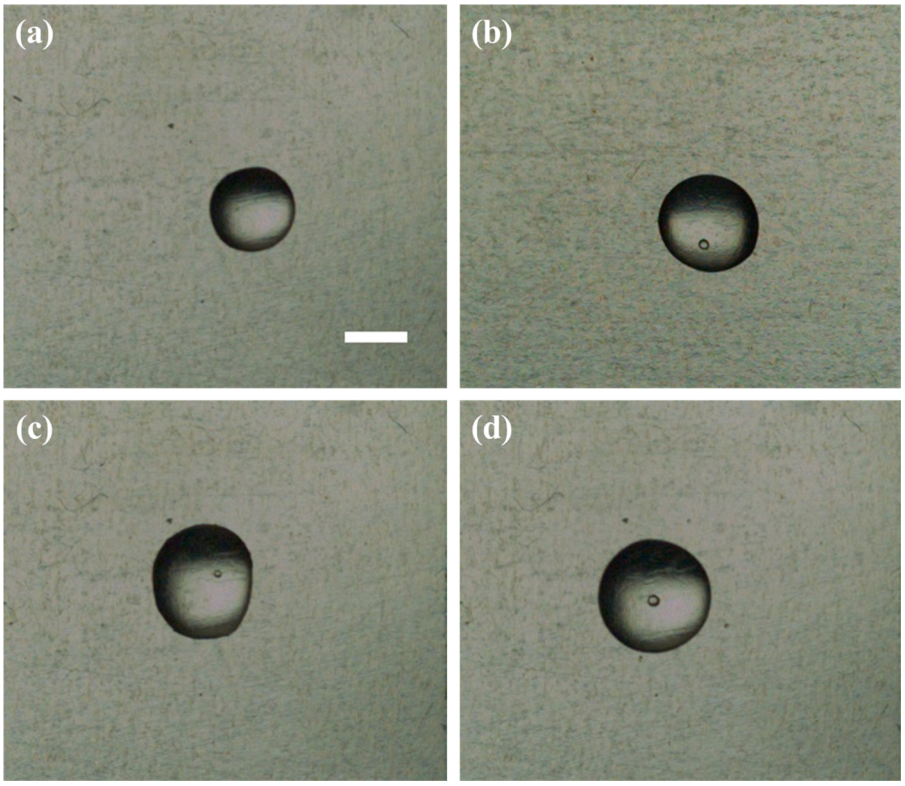


**Fig. 2.** Steady-state drop shapes after impacting onto parafilm substrate with air bubble entrapped. Drop sizes: (a) 2.20 mm, (b) 2.50 mm, (c) 2.65 mm and (d) 3.07 mm. The impact velocity is approximately 1.45 m·s$^{-1}$. Scale bar is 2 mm.

the interface and modifies the general NS equations to account for the two-phase flow effects in the PFM method. The chemical potential is dependent on the interfacial thickness; therefore, the surface-tension related body force is not constant during the liquid drop shape evolution. To keep the total free energy of the system constant, the variation due to the change in the surface-tension force is balanced by properly adjusting the interface thickness and thus, by adjusting the phenomenological mobility ($M_{\bar{c}}$).

### 2.3. Boundary conditions

Considering the surface to be ideal and the impact to be exactly perpendicular to the surface, axial symmetry can be assumed for the modeling purpose and so a 2D axisymmetric physical domain is considered. The dynamics of the contact line in the phase-field formulation is very important and several approaches have been proposed to study this (Alpak et al., 2016; Bai et al., 2017; Ding and Spelt, 2007; Zhang et al., 2016). The wetting (contact angle) boundary condition for the advective CH equation is expressed in the form of the geometrical formulation. In this formulation, for a given prescribed contact angle $\theta_s$ the wetting condition is given by Ding and Spelt (2007)

$$\mathrm{n}\cdot\varepsilon\nabla\bar{\mathrm{c}} = -\varepsilon\cos(\theta_s)|\nabla\bar{c}| \tag{7}$$

Additionally, it is required to use the non-penetration boundary condition at the solid surface while solving the CH equation (Eq. (4))

$$\mathbf{n}\cdot\nabla\varphi = 0 \tag{8}$$

Eq. (8) implies that the chemical potential flux does not penetrate through the solid surface. At the solid parafilm surface, the no-slip boundary condition is applied,

$$\mathbf{u} = 0 \tag{9}$$

The open boundary conditions are used at all other boundaries. This is implemented in the model by imposing a pressure at the free surface, i.e., at the boundary, while keeping the normal outflow velocity zero.

*Computational implementation.* The model is simulated in the COMSOL Multiphysics software version 5.5 using CFD module implementing phase-field and laminar flow. The adaptive mesh algorithm with the gradient of PFM variable as the error indicator, as well as the adaptive time stepping (backward differentiation formula) are used. The PFM variable $\bar{c}$ changes only across the interface between the liquid drop and air, and thus it is suitable for use as an error indicator during the computations. While using the adaptive meshing, both longest edge refinement and general modification methods are implemented. Considering finite element method scheme, the longest edge of the element is divided into two equal pieces while using longest edge refinement. In the general modification approach, the elements are made more isotropic by moving mesh vertices and collapsing elements that are too small to coarsen the mesh and thereby eliminating some poor-quality elements by creating new elements. It is found that using the general modification approach makes the simulation faster and time efficient than using longest edge refinement. The details of the analysis are provided in the supplementary material. The MUMPS (COMSOL, 2018) solver which is used to solve the system of linear equations for a finite element problem, is implemented to solve the initialization stage and the transient stage.

## 3. Results

In this section, first the experimental observations are analyzed, followed by the numerical results. The results of the two studies are compared by considering the evolution of the drop, the maximum spreading, and the formation of the air bubble.

### 3.1. Experimental results

Individual water drops are dripped onto the parafilm substrate from a fixed height of 11.5 cm in the case of the experiments of the first type.

**Table 1**
Effect of drop size on bubble entrapment.

| V (m/s) | D (mm) | We | Fr | Presence of bubbles (out of 10 trials) |
|---|---|---|---|---|
| 1.45 ± 0.01 m/s | 2.20 ± 0.01 mm | 63.41 ± 1.18 | 97.51 ± 1.56 | 3/10 |
| 1.47 ± 0.01 m/s | 2.50 ± 0.01 mm | 74.05 ± 1.32 | 88.20 ± 1.37 | 7/10 |
| 1.44 ± 0.01 m/s | 2.65 ± 0.01 mm | 75.33 ± 1.35 | 79.84 ± 1.26 | 7/10 |
| 1.44 ± 0.01 m/s | 3.07 ± 0.01 mm | 87.26 ± 1.52 | 68.92 ± 1.07 | 10/10 |

The top view recorded by a high-speed camera captured the impact and evolution of the drops at a rate of 1000 fps. Fig. 2 depicts the recorded steady-state shapes of the drops after they impacted onto the parafilm surface. It should be emphasized that the average drop diameters reported in Fig. 2 were measured from the side views recorded by a high-speed camera while drop was in flight in air before impact onto the parafilm surface. Accordingly, all average drop diameters have a standard deviation of ±0.01 mm.

The maximum spreading occurrs within the first few milliseconds after the drop impact. During the recoil stage, surface tension pulls the liquid back and the drops reach an equilibrium state, as shown in Fig. 2. Ten consecutive trials are conducted for each of the drop sizes studied. After each trial, the remaining liquid was removed by placing task wipers over the drop without rubbing the surface to avoid scratches on the parafilm surface. Among them, only 3 out of 10 trials reveal a bubble entrapped in the case of drop diameters of 2.20 mm. Moreover, 7 out of 10 trials reveal bubble entrapment in the case of drop diameters of 2.50 mm and 2.65 mm. In the case of drops of 3.07 mm diameter, all the trials reveal a bubble entrapped, as shown in Fig. 2d. The experimental results demonstrate that, as the drop diameter is increased, the higher is the probability of air being entrapped after drop impact onto parafilm surface, as shown in Table 1. Note that the different top-view drop shapes in Fig. 2 are due to the uncontrollable drop oscillations in flight before the drop impacts onto the parafilm surface. Thus, the initial contact that each drop makes with the solid surface slightly varies from trial to trial.

The remaining 9 trials conducted with the drop diameter of 2.65 mm (Fig. 2c) revealed a combination of circular and non-circular drop shapes with a predominance of the circular ones. The effect of the substrate roughness on the receding motion of the contact line explains the difference in the drop footprints shown in Fig. 2. Also, the snapshots captured in panels a through d in Fig. 2 represent the most repeatable bubble position in each trial for each drop diameter studied experimentally.

Similarly, in the experiments of the second type, individual water drops of a fixed diameter of ~2.50 mm drip onto the parafilm substrate from four different heights. Hence, four different impact velocities, 1.08 $m{\cdot}s^{-1}$, 1.47 $m{\cdot}s^{-1}$, 2.05 $m{\cdot}s^{-1}$ and 2.37 $m{\cdot}s^{-1}$, are explored. It should be emphasized that these impact velocities are the average values of ten trials conducted for each impact height. The top view recorded by a high-speed camera capture the impact and evolution of drops at a rate of 1000 fps. Fig. 3 depicts the recorded steady-state shapes attained by the drops after their impact onto the parafilm surface.

The equilibrium shapes of the drops shown in panels (a), (b) and (c) in Fig. 3 reveal bubble entrapment. Here, 9 trials out of 10 capture a bubble entrapped in the case of drops with an impact velocity of 1.05 $m{\cdot}s^{-1}$. Moreover, 7 trials out of 10, and 6 trials out of 10 capture a bubble entrapped for the impact velocities of 1.47 $m{\cdot}s^{-1}$ and 2.05 $m{\cdot}s^{-1}$, repectively. On the other hand, none of the ten trials reveal bubble entrapment in the case of the highest impact velocity of 2.37 $m{\cdot}s^{-1}$.

**Table 2**
Effect of drop velocity on bubble entrapment.

| V (m/s) | D (mm) | We | Fr | Presence of bubbles (out of 10 trials) |
|---|---|---|---|---|
| 1.08 ± 0.01 m/s | 2.50 ± 0.01 mm | 39.97 ± 0.91 | 47.60 ± 0.97 | 9/10 |
| 1.47 ± 0.01 m/s | 2.50 ± 0.01 mm | 74.05 ± 1.32 | 88.20 ± 1.37 | 7/10 |
| 2.05 ± 0.01 m/s | 2.50 ± 0.01 mm | 144.02 ± 2.00 | 171.53 ± 2.01 | 6/10 |
| 2.37 ± 0.01 m/s | 2.50 ± 0.01 mm | 192.50 ± 2.42 | 229.26 ± 2.39 | 0/10 |

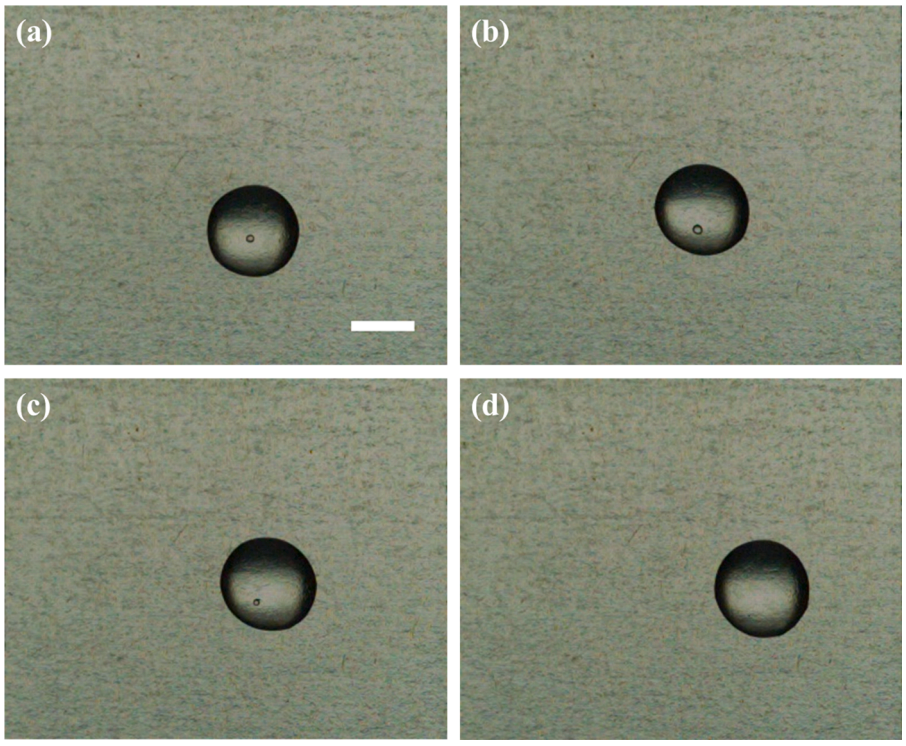


**Fig. 3.** Steady-state drop shapes after impact onto parafilm substrate with air bubble entraped. The impact velocities: (a) 1.08 $m{\cdot}s^{-1}$, (b) 1.47 $m{\cdot}s^{-1}$, (c) 2.05 $m{\cdot}s^{-1}$, and (d) 2.37 $m{\cdot}s^{-1}$. Drop diameter is approximately 2.50 mm. Scale bar is 2 mm.

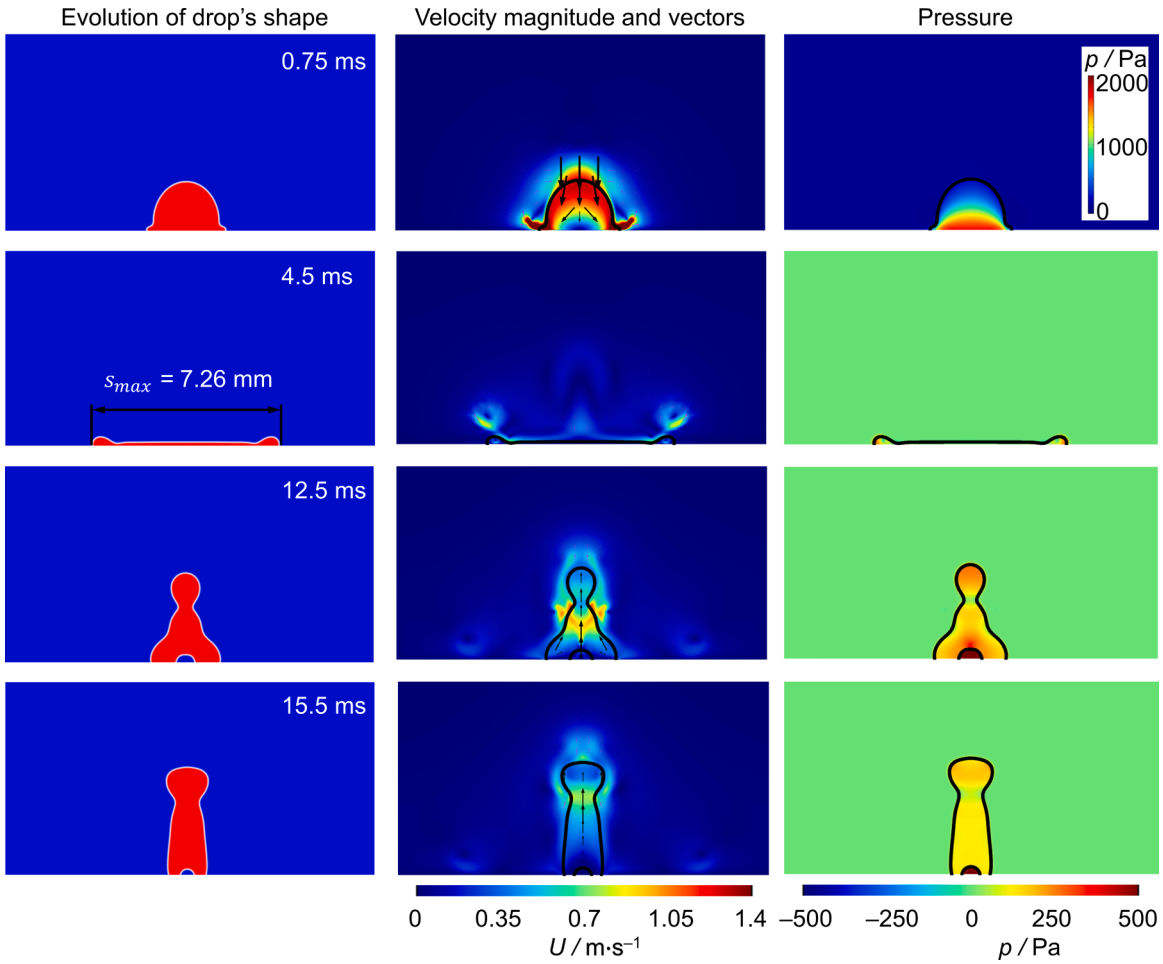


**Fig. 4.** (Left-hand side column) Median cross-section of the predicted drop. Blue color corresponds to air, and red color corresponds to water drop. (The middle column) Velocity vectors. (The right-hand side column) Pressure field evolution during the drop impact. The drop diameter is 2.5 mm, and the initial drop velocity is 1.45 m·s$^{-1}$ (For interpretation of the references to color in this figure legend, the reader is referred to the web version of this article).

These results demonstrate that as the impact velocity is increased, the lower is the probability of air being entrapped after drop impact onto parafilm surface, as shown in Table 2.

### 3.2. Modeling results

#### 3.2.1. Parametrization

For the CHNS simulations, the parameters used are the phase-field mobility, the interface thickness, the viscosity and density of both the phases, the drop radius and the impact velocity. Ideally, energy dissipation across the interface can be reduced by decreasing the diffuse interface thickness. Moreover, smaller thickness will lead to lower mass loss of the drop as the interface thickness is directly proportional to the drop shrinkage. However, the interface thickness should be selected considering computational cost and capability to achieve accurate results efficiently. Furthermore, based on our prior experience with COMSOL, there should be at least two quadratic triangular mesh elements across the interface between the two fluids for proper interface development. Overall, the interface thickness should be chosen considering that the numerical solution of the phase-field variable is smooth enough to express the diffusive interface and the solution is numerically converged both in the fluid's bulk and on the interface with reasonable time step size. The CHNS model is run using proper adaptive mesh algorithm with an adaptive time step size to satisfy the above-mentioned criteria. The adaptive mesh approach correctly tracks the moving interface and increases the resolution of the mesh locally at the interface to a predefined acceptable value at each time step to predict the evolution of the drop shape properly. If an adaptive mesh algorithm is not implemented, then a very finely structured mesh is used in the entire modeling domain to obtain accurate results. For all present calculations the interface thickness is 40 μm.

The phenomenological mobility, or conventionally known as phase-field mobility, $M_{\tilde{c}}$, is another significant parameter. This parameter is also known as the Onsager transport coefficient. In the CHNS modeling the phenomenological mobility is used to control both the interface movement and the shape of the drop. Thus, the parameter $M_{\tilde{c}}$ should be chosen appropriately; otherwise, the simulation solutions will not be physically correct. If $M_{\tilde{c}}$ is very large, then the diffusion term will over damp the flow and if it is too small, then the solution may not converge numerically. There is no exact formula to calculate the mobility; however, a good approach to select its value is through comparison with experimental results. A more elaborate discussion regarding the selection of the mobility tuning parameter and the interface thickness in the CHNS modeling is provided by Bai et al. (2017). In our work, the mobility was tuned to obtain a good agreement with the experimental measurements of the drop impact onto the solid surface in terms of time of maximum spread. As a result, the mobility value is taken as $4.8 \times 10^{-8}$ m$^3$·s·kg$^{-1}$.

Proper mesh resolution is required for every numerical simulation so that the solutions are mesh independent. The mesh resolution should be adequate to minimize the energy dissipation at the interface and for smooth transition of the physical parameters across the interface. The finite element method is used for the discretization of the governing equations in the numerical solution. The mesh is created using the

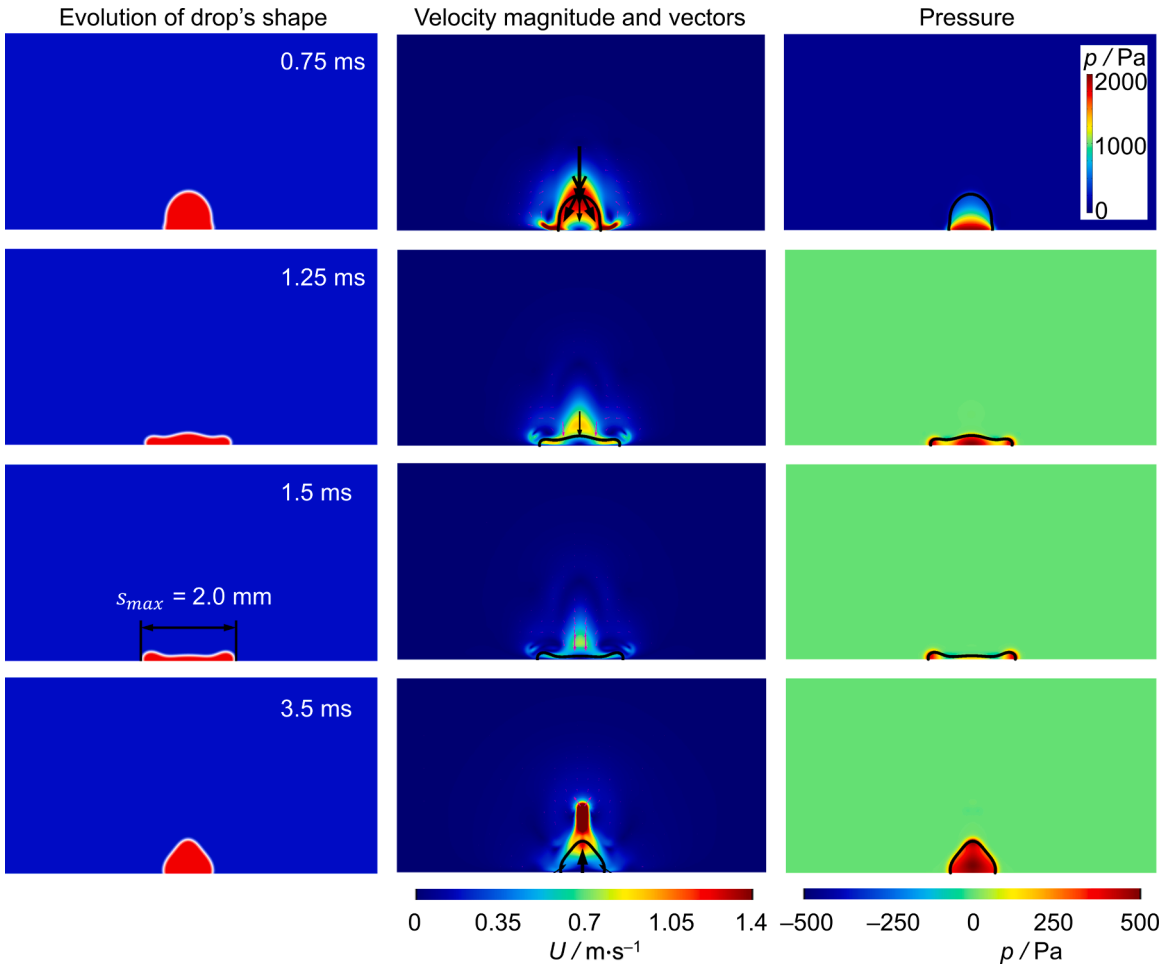


**Fig. 5.** (Left-hand side column) Median cross-section of the predicted drop. Blue color corresponds to air, and red color corresponds to water drop. (The middle column) Velocity vectors. (The right-hand side column) Pressure field evolution during the drop impact. The drop diameter is 1 mm, and the initial drop velocity is 1.45 m·s$^{-1}$ (For interpretation of the references to color in this figure legend, the reader is referred to the web version of this article).

COMSOL's inbuilt mesh building scheme. For conservation of the phase-field variable, at least two or three elements are kept within the air-drop interface and so the interface region has a very fine mesh. This is done by properly tuning the number of elements along the interface (the maximum element size of 0.0536 mm and the minimum element size of 0.00016 mm for a domain size of 8 mm × 14 mm which is used to obtain results in Fig. 4) to achieve optimum refinement along that surface. A coarser mesh is used in the domain consisting of air and a relatively finer mesh is used inside the liquid drop domain. A gradual change in the size of the elements from the interface to the rest of the domain is applied.

### 3.2.2. *Simulation results for formation of entrapped air*

The impact of water drop on hydrophobic parafilm surface is presented in this section. To model the phase-field interface, the thickness ($\varepsilon_{\bar{c}}$) of the interface is taken as 40 μm which is constant throughout the simulation. The mobility tuning parameter ($\chi$) is chosen by comparing with the experimental results and the value is 30 m·s·kg$^{-1}$.

The diameter of the water drop is taken to be 2.5 mm and the initial drop velocity is chosen to be 1.45 m·s$^{-1}$. This impact velocity is imposed on the entire drop uniformly and is perpendicular to the horizontal solid surface. The density, dynamic viscosity and surface tension coefficient ($\gamma$) of the water drop at 20 °C are 1000 kg·m$^{-3}$, 1 mPa·s and 72.0 mN·m$^{-1}$, respectively. The initial velocity of the surrounding air is set to zero.

At first, the proper adaptive mesh algorithm is selected to track the moving interface accurately, while keeping the computation time and memory as minimum as possible. Then, with the optimum settings all the simulations have been performed. It is found that the longest edge refinement adaptation scheme (0.06% mass change) is more efficient than the general modification adaptation scheme (1.51% mass change) considering the mass change. However, for both cases, the mass change is almost negligible. Another important fact to consider is the computational time. The general modification scheme takes considerably less computational time and storage than those of the longest edge refinement whereas the shapes of the drop at each time step for both the schemes are identical. Considering all the facts, the general modification method is chosen for all simulations.

The simulation results of drop impact, spreading and air bubble entrapment for water drop on parafilm surface are shown in Fig. 4 as a cross-section of a 2D axisymmetric domain. The left column in this figure represents the time evolution of the drop shape, with the blue color denoting the gas phase (surrounding air) and the red color referring to the water drop. The middle column represents velocity magnitudes and vectors, and the right column represents the pressure field over time. The maximum spreading distance ($s_{max}$) of the drop is 7.26 mm and it occurs at the time of 4.5 ms. The evolution of the drop morphology suggests that in the early stage of the spreading phase, there exists two parts for the drop: the outer rim and the middle shoulder. After the drop touches the parafilm surface, it spreads rapidly and forms an outer rim that continuously spreads during the first few milliseconds and reaches the maximum spreading after which the drop retracts due to hydrophobic nature of the surface. During the retraction phase there is a

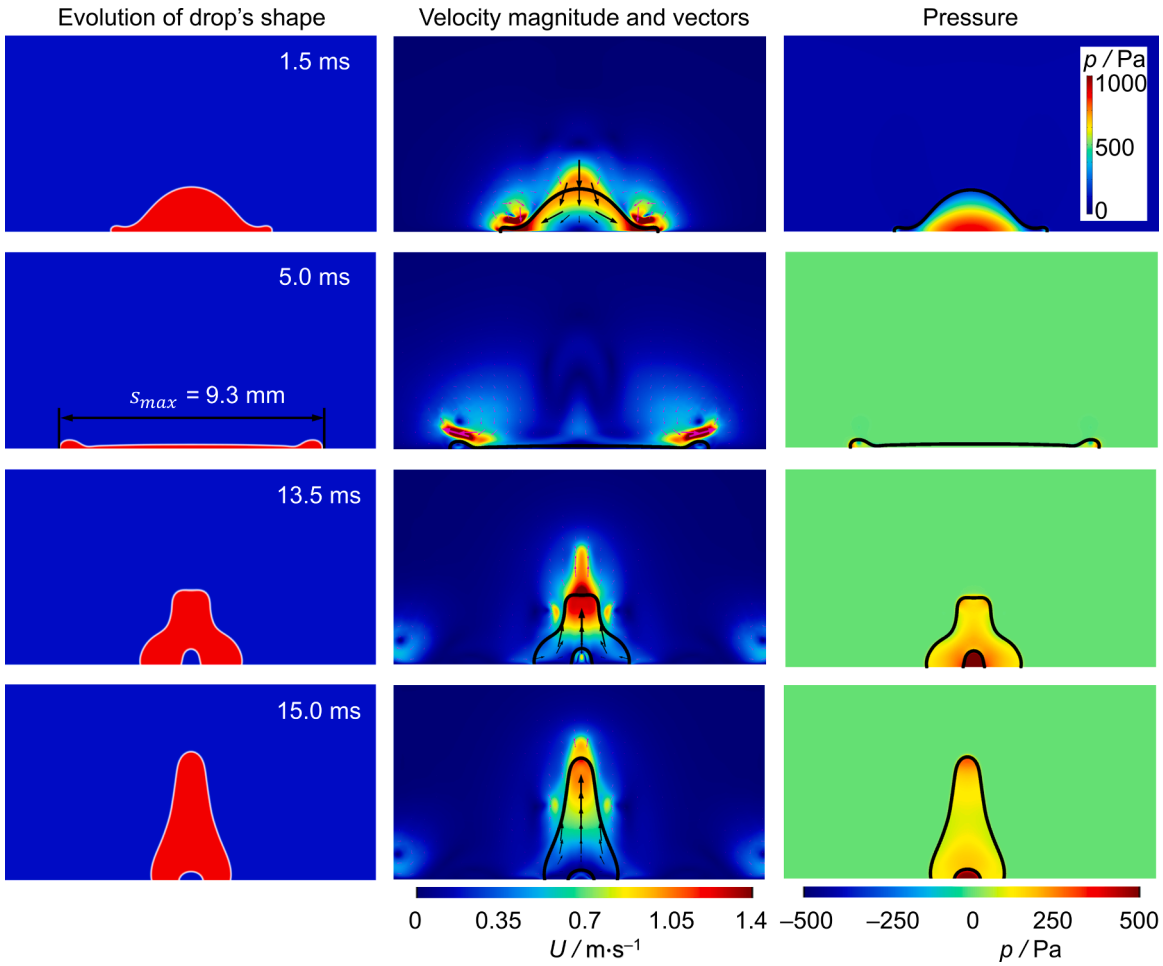


**Fig. 6.** (Left-hand side column) Median cross-section of the predicted drop. Blue color corresponds to air, and red color corresponds to water drop. (The middle column) Velocity vectors. (The right-hand side column) Pressure field evolution during the drop impact. The drop diameter is 3 mm, and the initial drop velocity is 1.45 m·s$^{-1}$ (For interpretation of the references to color in this figure legend, the reader is referred to the web version of this article).

formation of air cavity at the center of the drop and the top liquid layer of the drop encloses the cavity (see supplementary video) and thus an entrapped air bubble is formed.

Inspecting the velocity magnitudes and velocity vectors shown in the middle column of Fig. 4, it is observed that the velocity reaches the highest values at the initial moment of the drop impact and after that it decreases gradually. During the rebounding phase, there is the formation of a neck in the drop and the velocity magnitude is higher in that region than the rest and this necking leads to detachment and formation of a satellite drop (see supplementary video).

Next, the pressure field variation over time during the impact is analyzed (Fig. 4, right column). As expected, the maximum pressure is observed during the initial stages of the impact. In addition, it can be noticed that the pressure inside the air bubble is higher than the surrounding water drop pressure, which is responsible for the entrapped bubble to exist in the center of the drop.

### 3.2.3. *Effect of the drop diameter*

The diameter of the drop plays a significant role in the air bubble formation during the impact onto the solid hydrophobic surface. We have performed a series of calculations varying the drop diameter and studied how it affects the air bubble formation. Fig. 5 presents the results of 1 mm diameter water drop impact, similarly to Fig. 3 for the 2.5 mm diameter. The results shown in Fig. 5 suggest that when the diameter is decreased to 1 mm, the maximum spreading distance is reduced to 2 mm and no air bubble is observed. The results (not shown here) for a drop of diameter of 2 mm have also revealed no air bubble entrapment with a maximum spreading distance of 5.4 mm.

When the diameter is increased from 2.5 mm to 3 mm the maximum spreading distance increases to 9.3 mm and the air cavity is formed at the center of the drop during the retraction phase (Fig. 6). Therefore, for the same constant velocity, the air bubble is formed when the diameter of the drop is large enough. The maximum spreading distance is increased when the size of the drop is increased, and it takes a longer time to attain maximum spreading. Also comparing Figs. 4–6, it is observed when the diameter is increased a vortex is formed in the air, on each side of the drop during the spreading and the size of the vortex increases with increased diameter. This is because during the spreading a thick rim is formed at the edge of the drop which creates a circular motion of the surrounding air which creates the vortex. Since the open boundary condition is implemented for the simulation, the vortex eventually leaves the computational domain.

### 3.2.4. *Effect of the impact velocity*

In this analysis, the drop diameter is kept constant at 2.5 mm, and the impact velocity of the drop is varied. For impact velocity of 1.08 m·s$^{-1}$ the maximum spreading distance is reduced to 6.3 mm (Fig. 7) comparing to the case of 1.45 m·s$^{-1}$ impact velocity (cf. Fig. 4). Also, in this case, an air bubble is formed at the center.

Fig. 8 shows the simulation results when the impact velocity is 2.37 m·s$^{-1}$. For this case the maximum spreading distance is increased to 8.7 mm significantly larger than that in the previous case. For this higher impact velocity, no air cavity is observed. Thus, for a constant size of the drop when the velocity is low there is a higher probability of air bubble

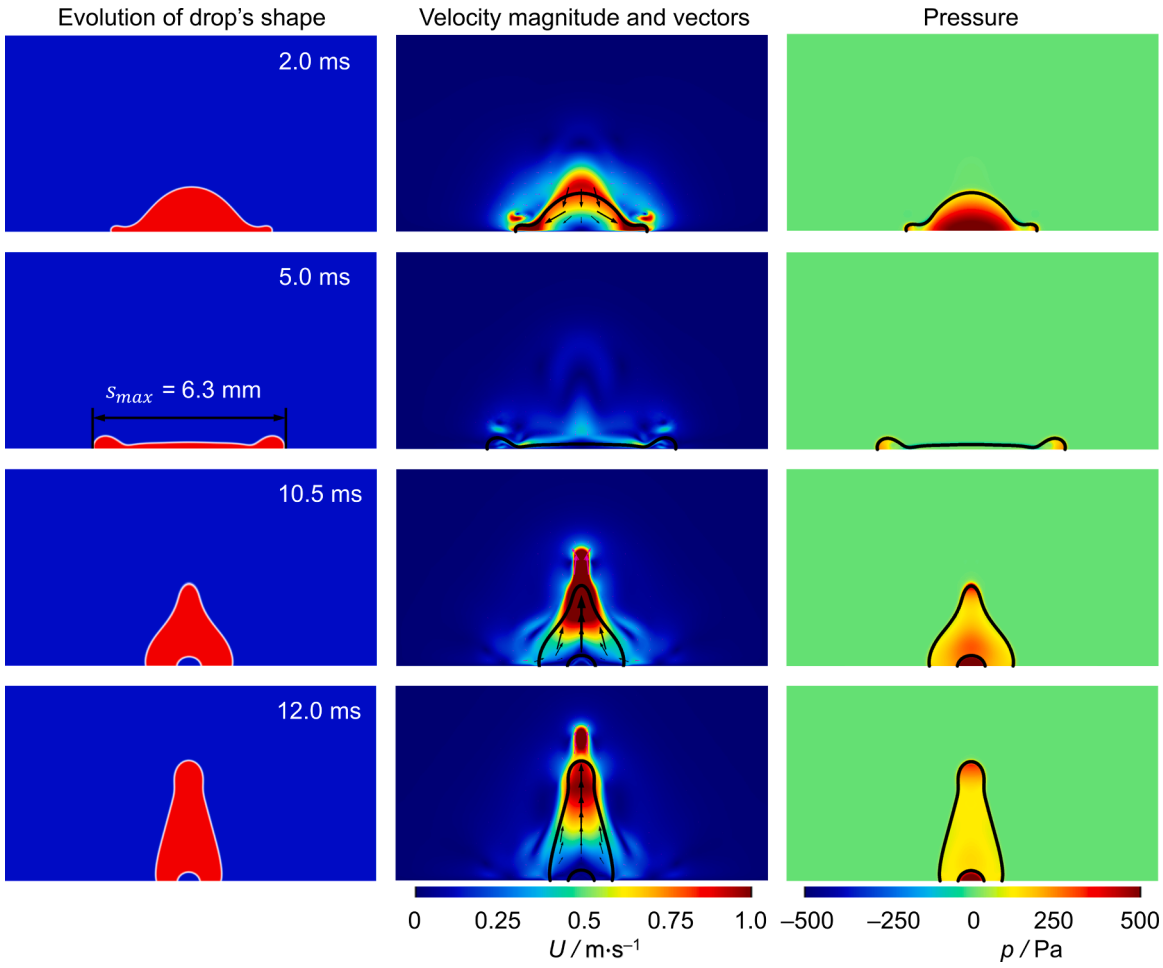


**Fig. 7.** (Left-hand side column) Median cross-section of the predicted drop. Blue color corresponds to air, and red color corresponds to water drop. (The middle column) Velocity vectors. (The right-hand side column) Pressure field evolution during the drop impact. The drop diameter is 2.5 mm, and the initial drop velocity is 1.08 m·s$^{-1}$ (For interpretation of the references to color in this figure legend, the reader is referred to the web version of this article).

formation. It can be concluded that to avoid air entrapment, the impact velocity must be high. Moreover, the maximum spreading distance is increased with the increase of the impact velocity, and it reaches the maximum spread condition faster. For higher impact velocities, a vortex is formed, which becomes larger with increasing the velocity.

### 3.2.5. Sensitivity analysis

Additionally, we have performed a sensitivity study of the mobility tuning parameter and the interface thickness similarly to that in (Fink et al., 2018; Yurkiv et al., 2018). Specifically, we changed these parameters to observe the change in the maximum spreading distance keeping the drop diameter and the impact velocity constant at 2.5 mm and 1.45 m·s$^{-1}$, respectively. Six cases are selected for checking the sensitivity of the model: (i) increasing the interface thickness from 40 to 44 μm (10%), (ii) increasing the mobility tuning parameter from 30 to 33 m·s·kg$^{-1}$ (10%), (iii) increasing both the interface thickness and the mobility tuning parameter by 10%, (iv) decreasing the interface thickness from 40 to 36 μm (10%), (v) decreasing the mobility tuning parameter from 30 to 27 m·s·kg$^{-1}$ (10%), and (vi) decreasing both the interface thickness and the mobility tuning parameter by 10%. The results show that for the first case the maximum spreading distance decreases from 7.26 mm to 7.22 mm, and for the second case it decreases to 7.24 mm. For the third case, the maximum spreading distance changes to 7.20 mm, which is the most significant among all, whereas, for cases (iv), (v) and (vi) the maximum spreading distance increases to 7.30 mm, 7.27 mm and 7.32 mm, respectively. Consistent with the results of Bai et al. (2017), it is observed that small changes in the values of $\varepsilon_{\tilde{c}}$or $\chi$ do not lead to noticeable changes in the drop shape prediction; however, if they are changed together it could lead to a larger change. Such small changes in the maximum spreading distance are almost negligible with respect to the changes in the phase field parameters. As mentioned by Bai et al. (2017), here we can similarly observe that the mobility $(M_{\tilde{c}})$ which is the product of the tuning mobility and the square of the interfacial thickness, must be kept constant to predict the physical process accurately. When the mobility tuning parameter and the interface thickness are varied by an equal percentage, the variation in the mobility is higher for the latter case. Hence, the interface thickness has a slightly more pronounced effect on the simulation results than the mobility tuning parameter does. Additionally, the effect of the Cahn number ($Cn$), which is the ratio of the interface thickness and the drop diameter (Wörner et al., 2021), on the maximum spreading distance is analyzed. In all the simulations the range of the values of $Cn$ varies from 0.0095 to 0.04. From the simulations, two cases with drop diameters of 3 mm ($Cn = 0.013$) and 1 mm ($Cn = 0.04$) are chosen. The impact velocity and the mobility tuning parameter ($\chi$) are kept constant at 1.45 m·s$^{-1}$ and 30 m·s·kg$^{-1}$, respectively. In the first case, the interface thickness is changed to 60 μm, resulting in $Cn = 0.02$. The maximum spreading distance is found to be 9.1 mm, compared to 9.3 mm for Cn = 0.0133. In the second case, the interface thickness is changed to 20 μm, resulting in $Cn = 0.02$, and the maximum spreading distance is found to be 2.1 mm, compared to 2.0 mm for $Cn = 0.04$. This shows that the effect of the change in the value of $Cn$-number in our cases is small and the results are almost similar.

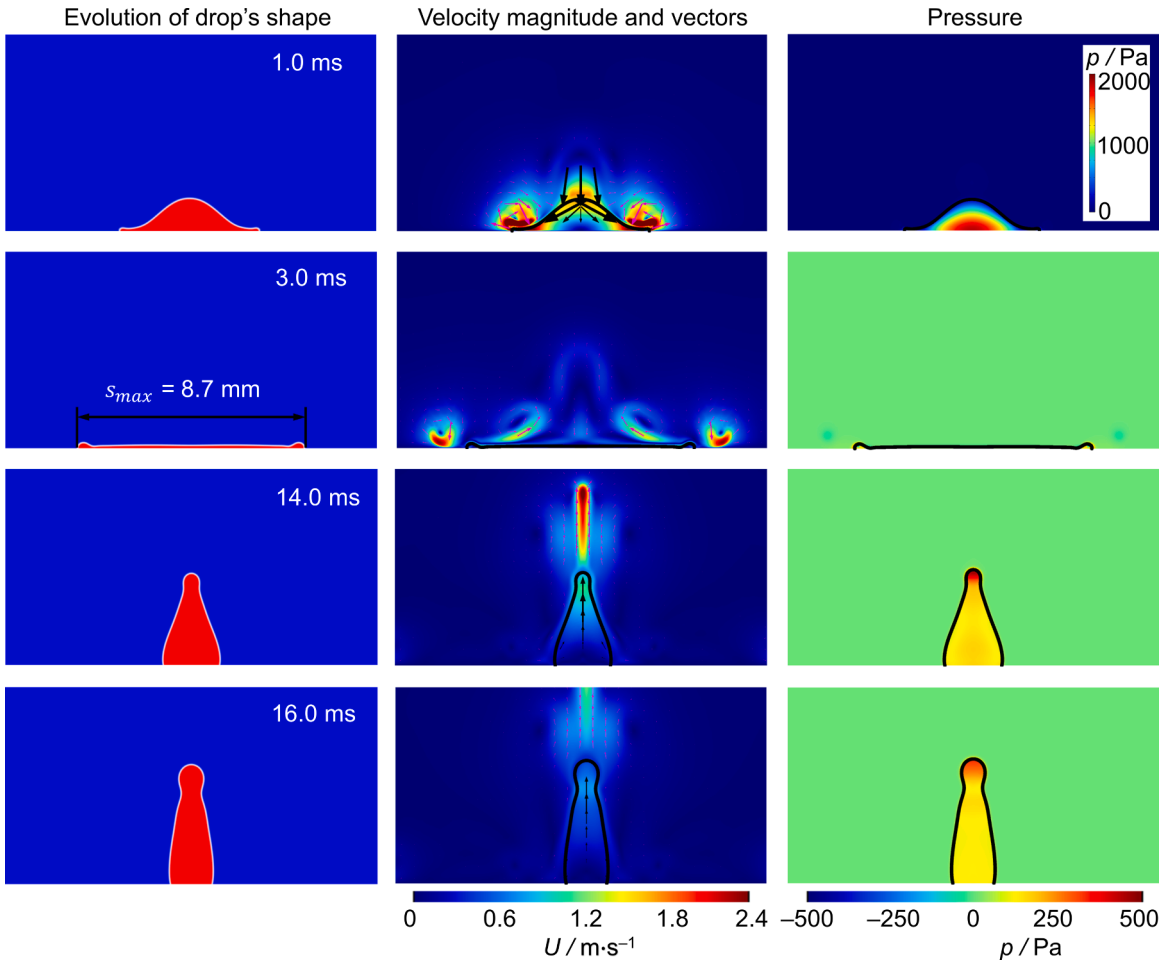


**Fig. 8.** (Left-hand side column) Median cross-section of the predicted drop. Blue color corresponds to air, and red color corresponds to water drop. (The middle column) Velocity vectors. (The right-hand side column) Pressure field evolution during the drop impact. The drop diameter is 2.5 mm, and the initial drop velocity is 2.37 m·s$^{-1}$ (For interpretation of the references to color in this figure legend, the reader is referred to the web version of this article).

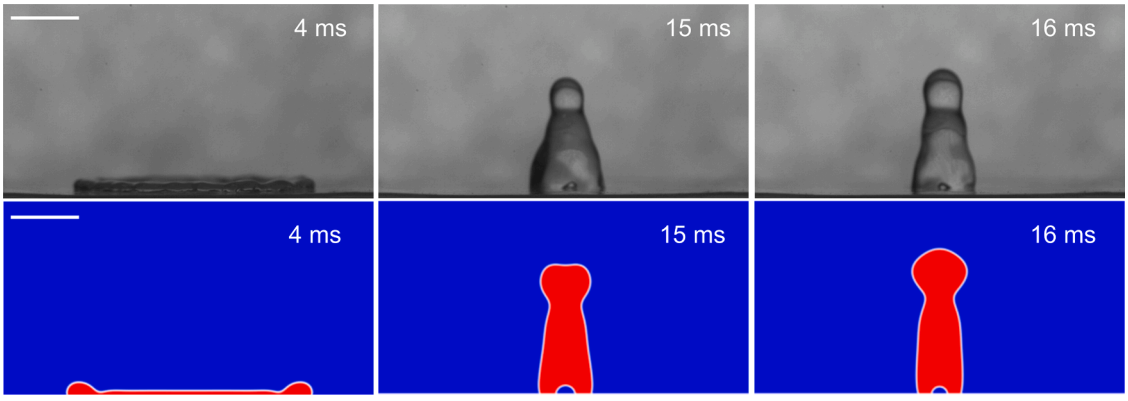


**Fig. 9.** Comparison between (upper row) the experimentally observed shapes and (bottom row) the predicted drop shapes at different times. The drop diameter is 2.5 mm, and the initial drop velocity is 1.45 m·s$^{-1}$. Scale bar is 2 mm.

*3.2.6. Comparison between the experiment and the simulation results*

In this section the numerical and the experimental results are compared for a case with drop diameter 2.5 mm and impact velocity 1.45 m·s$^{-1}$. Fig. 9 shows that the model predicts the drop shapes almost similarly to those observed experimentally. The maximum spreading distance is 7.26 mm in the simulation whereas it is 7.14 mm in the case of the experiment. The maximum spreading distance can also be calculated from the value of *We* using the theoretical formula proposed by Pasandideh-Fard et al. (1996):

$$\frac{D_{\max}}{D_0} = \sqrt{\frac{We + 12}{3(1-\cos\theta) + 4\left(\frac{We}{\sqrt{Re}}\right)}} \tag{10}$$

where $D_{\max}$ is the maximum spreading diameter, and $D_0$ is the initial drop diameter. From the formula, the maximum spreading has been predicted to be 7.88 mm compared to 7.26 mm in our simulation, which reveals a good agreement of our simulation results with the prior

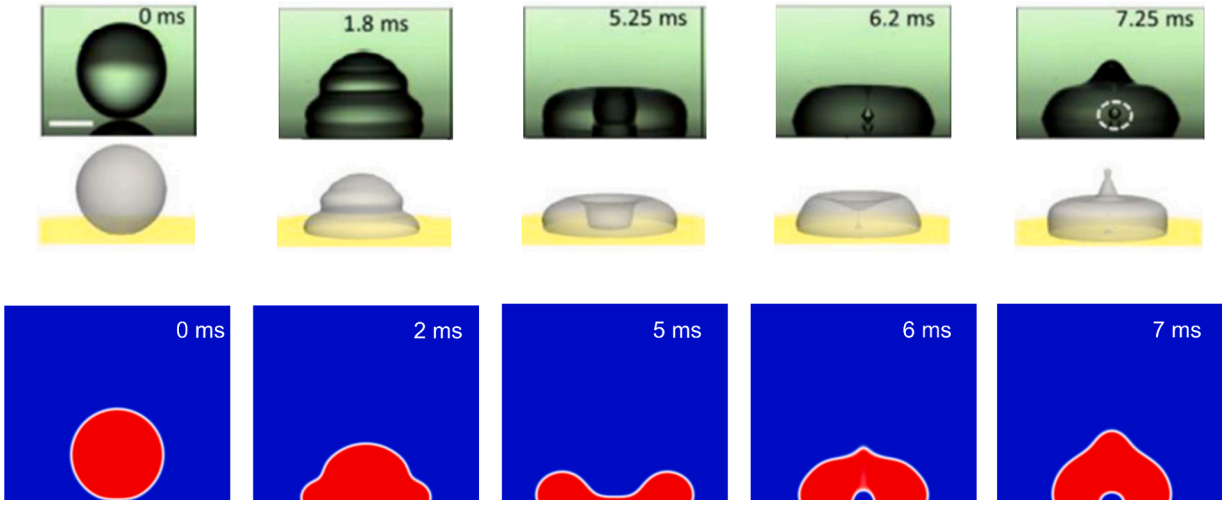


**Fig. 10.** Comparison between the experimental results of Lin et al. (2018) (upper row), simulation results of Wörner et al. (2021) (middle row) and our own numerical simulations (bottom row). The drop diameter is 2 mm, and the initial drop velocity is 0.52 m·s$^{-1}$. Scale bar is 1 mm.

theoretical estimate.The numerical simulation is able to predict the formation of air bubble in the center of the drop as seen in the experiment. However, an exact comparison of the drop shape is almost impossible because the present simulation is axisymmetric whereas there is a deviation from the axial symmetry in the experiment. Also, the exact morphology of the surface is not replicated in the simulation, and this may affect the shapes of the drop at different stages. Consequently, rather than a quantitative comparison, a qualitative comparison between the simulation and the experiment is more reasonable.

To further validate our model, it has been extended to reproduce the results of Wörner et al. (2021), where the drop diameter is 2 mm and the contact angle and impact velocity are 106° and 0.52 m·s$^{-1}$, respectively. Fig. 10 shows that the predicted shapes obtained from our model are in good agreement with the simulation results reported by Wörner et al. (2021) and the experimental observations of Lin et al. (2018). The present simulation also correctly predicts the air bubble formation as seen in the figure.

### 3.2.7. Bubble formation in terms of We and Fr

In this section, the following non-dimensional numbers are used to characterize the bubble formation:

$$We = \frac{2\rho U^2 R}{\gamma}, \; Fr = \frac{U^2}{2gR} \tag{11}$$

Here, $R$ is the initial volume-equivalent radius of the drop (characteristic length) and $U$ is the reference velocity (impact velocity). These two parameters are sufficient for the study of the impact event when the drop is assumed to be spherical during the moment of impact (Hasan and Prosperetti, 1990). The Weber number (*We*) is a dimensionless number that is frequently used for analysis of multiphase fluid flows particularly when there is a curved interface between two different fluids. It is a measure of the relative importance of the fluid's inertia and the surface tension force. The Froude number (*Fr*) is defined as the ratio of the flow inertia to the gravitational force. The *We* is varied from 27 to 230 and the *Fr* is varied from 35 to 300 approximately. In addition to that the Reynolds number or *Re* $\left(\frac{\rho UR}{\mu}\right)$ varies from 720 to 4080 for all simulated cases. Fig. 11 shows that the results of the numerical simulation are in close agreement with the experimental observations on a *We*-*Fr* plane. A low *Fr* means that either the velocity is low, or the diameter is large and for both of these cases there is a high probability of bubble entrapment. However, when the *Fr* is increased due to an increase in velocity or decrease in diameter, the chances of air bubble entrapment decreases,

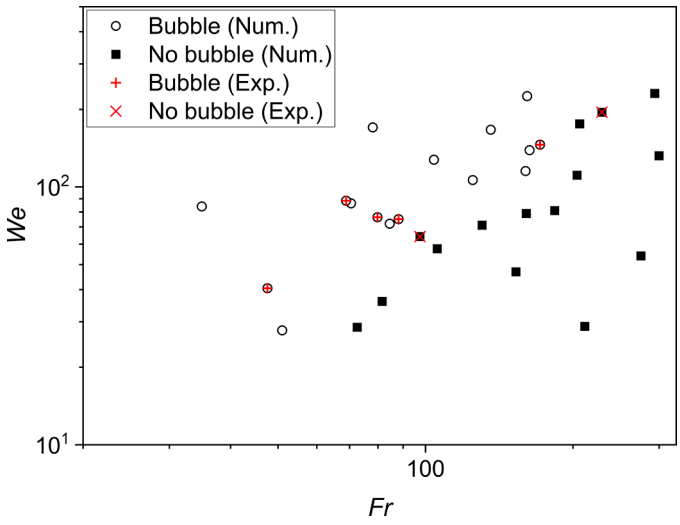


**Fig. 11.** Bubble formation as a function of *We* and *Fr*.

and it can be seen from Fig. 11 that at very large *Fr* there is no bubble formation. When the *We* is high due to larger drop size then the *Fr* is low (top left region of Fig. 11) and in this region air bubble formation is more prominent. On the other hand, when the *We* is high due to larger impact velocity then the *Fr* is high (top right region of Fig. 11) and in this region there is no formation of air bubble. Finally, when the *We* is increased, a higher *Fr* is needed to achieve drop impact without bubble. There is a maximum limit of how large the *We* or the *Fr* can be as the maximum impact velocity is equal to the terminal velocity of the corresponding drop and the terminal velocity is dependent on the drop size. Though some regions in Fig. 11 do not have sufficient data points, the trend is considered to be continuous as the probability of air bubble formation always increases with an increase in drop diameter or a decrease in the impact velocity.

### 3.2.8. Drop impact onto water surface

Finally, the model is modified to simulate the case when the drop impacts onto a water surface. The simulation results are validated with results of Hasan and Prosperetti (1990). The drop diameter is 3.8 mm and the impact velocity is 1.53 m·s$^{-1}$. The problem is considered axisymmetric, and the flow is laminar. To model the phase-field interface, the thickness ($\varepsilon_{\tilde{c}}$) of the interface is set equal to 40 μm. Fig. 12

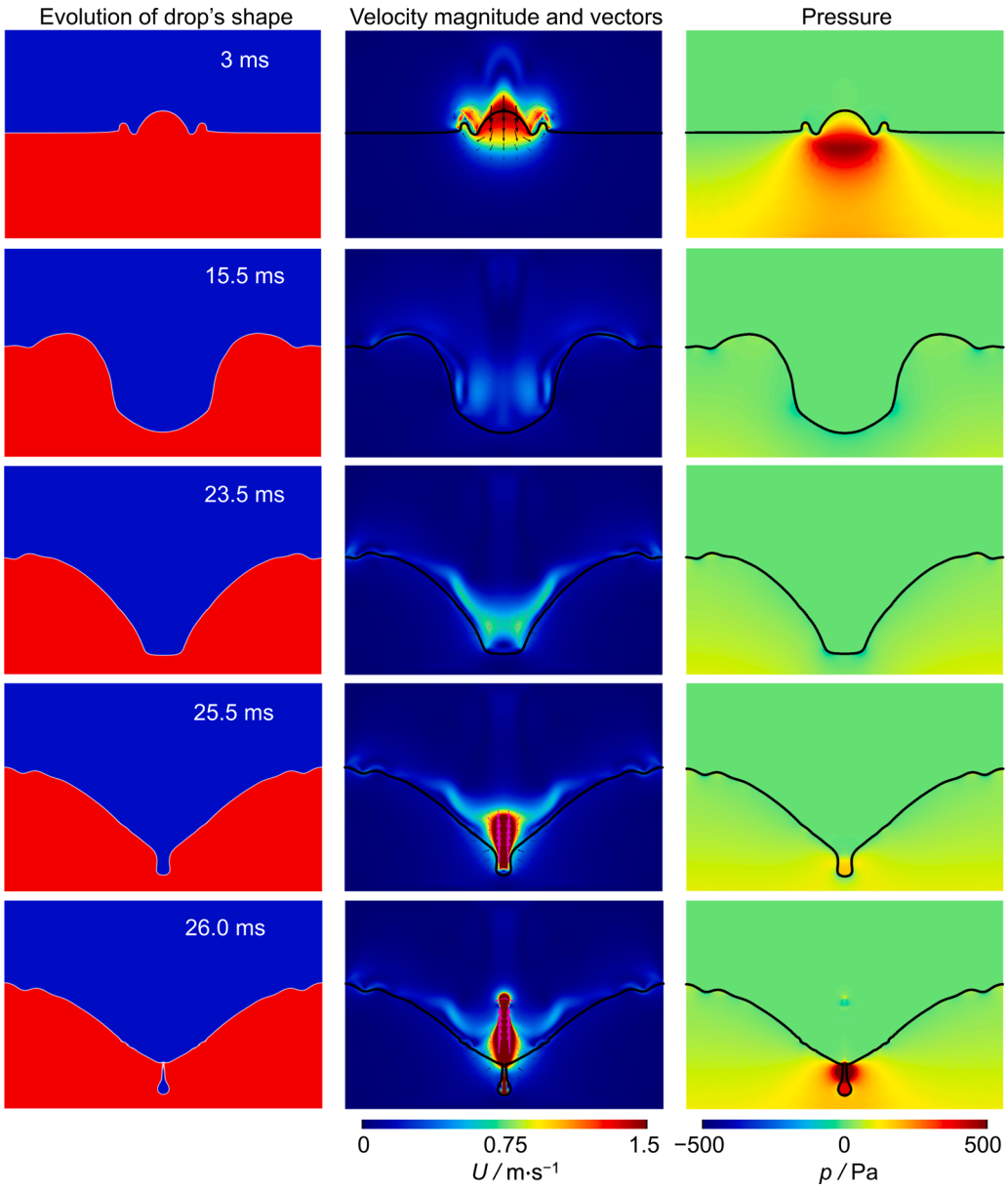


**Fig. 12.** (Left-hand side column) Median cross-section of the predicted crater. Blue color corresponds to air, and red color corresponds to water drop. (The middle column) Velocity vectors. (The right-hand side column) Pressure field evolution during the drop impact. The drop diameter is 3.8 mm, and the initial drop velocity is 1.53 m·s$^{-1}$ (For interpretation of the references to color in this figure legend, the reader is referred to the web version of this article).

shows that due to the drop impact, a crater is formed in the water surface. Initially, the cavity has an almost cylindrical shape with a rounded nose. Then, the motion of the liquid at the perimeter of the crater stops and reverses its direction at different times along the depth of the crater. Though the tip of the cavity keeps growing, the sidewalls reverse their outward motion and start moving in the inward direction with a velocity that increases with depth. As a consequence of this situation, there is a formation of a peculiar funnel shape in the last few steps, which leads to an air bubble entrapment during the pinching-off of the narrow tip. There is a significant increase of pressure inside the air bubble formed at the tip.

The results are validated by comparison with the experimental results of Pumphrey and Walton (1988) and the numerical simulation of Hasan and Prosperetti (1990) (cf. Fig. 13). It is seen that the model is in good agreement with the experimental data and the prior numerical simulations conducted using the boundary-integral method. The initial time step is different because the initial height of the drop over the free water surface is considered different for our present model and the experimental results. Moreover, rather than a quantitative analysis a qualitative comparison is more sensible. This further validates that the present model is accurate and can be used for similar drop related problems. Moreover, it can be seen that high pressure build up inside the air bubble is common for both cases (impacts on solid or liquid surfaces) and it is one of the main reasons for the entrapped air bubble to keep intact. The difference is that for solid surface the velocity magnitude near the bubble is constant (Fig. 4) whereas for liquid surface the velocity magnitude is higher in the bubble region and the direction of the flow is upward (Fig. 4). This is because for the impact on solid surface, the bubble is formed on top of the parafilm surface where the liquid velocity is zero considering the no-slip boundary condition but for the liquid surface, the top layer is moving and the direction of the flow is upward during the time of air entrapment. The current model is able to predict the shapes in both situations

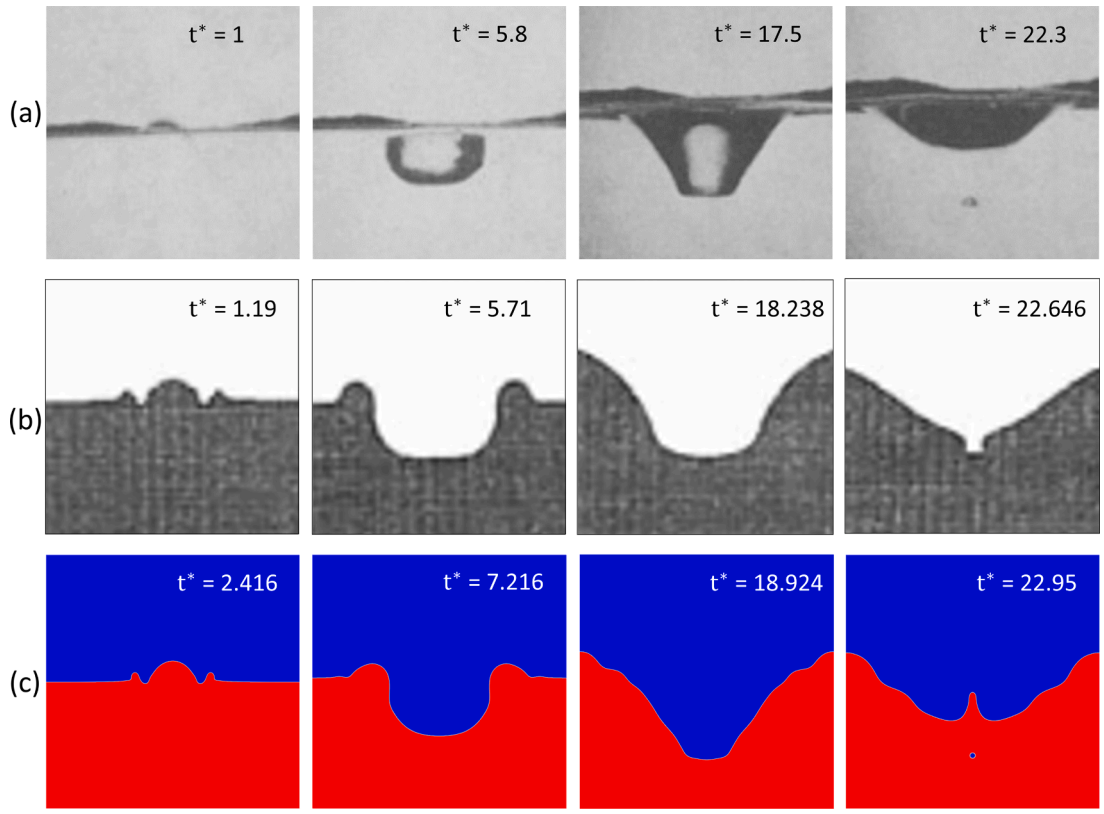


**Fig. 13.** Comparison between (a) experimental results of (Pumphrey and Walton, 1988), (b) numerical results of (Hasan and Prosperetti, 1990) and (c) model's prediction. The drop diameter is 3.8 mm, and the initial drop velocity is 1.53 m·s$^{-1}$. The times are in the dimensional units $t^* = \frac{tU}{R}$.

## 4. Conclusion

In this work, the air bubble formation during the water drop impact on a solid hydrophobic Parafilm surface has been discussed along with experimental validation. The coupled Cahn-Hilliard and Navier-Stokes equations, usually referred as the CHNS equations, are used for the numerical simulation. The two-phase flow is considered to be laminar and the interface between the two fluids has a finite thickness. The adaptive mesh algorithm which is required to track the moving interface in a two-phase flow has been discussed in detail. In addition, the application of the non-conservative and conservative forms of the CH equation and its impact on the mass loss of the system has been analyzed. The significance of the phase-field parameters (interface thickness and mobility tuning parameter) while predicting the time evolution of the drop shape has also been studied. It is found that the mobility value must be chosen for a PFM model by a trial-and-error approach (comparison with experimental results) for a specific problem.

The model successfully predicts the drop shape in a qualitative agreement with the experimental results. The model reveals that for water drop impact on a hydrophobic parafilm surface there is a chance of air bubble entrapment during the retraction phase. The effects of the drop diameter and the impact velocity are studied. It is found that for a constant drop diameter, decreasing the velocity leads to a higher chance of formation of air bubble. Similarly, increasing the diameter while keeping the velocity constant, leads to a higher chance of formation of air bubble.

Furthermore, the proposed model is also able to accurately predict air bubble entrapment following water drop impact onto water surface, which creates an expanding and collapsing crater. The latter case was validated by comparison with the experimental data and numerical simulations from literature.

In addition, it is found that the mobility in a PFM model should be calculated by a trial-and-error approach (comparison with experimental results) for a specific problem, as it has been done in the above-mentioned simulations.

## CRediT authorship contribution statement

**Subhayan Halder:** Conceptualization, Methodology, Software, Writing – original draft, Writing – review & editing, Visualization, Formal analysis. **Rafael Granda:** Methodology, Validation, Writing – original draft, Validation, Investigation. **Jingwei Wu:** Methodology, Validation, Investigation. **Abhilash Sankaran:** Methodology, Validation, Investigation. **Vitaliy Yurkiv:** Methodology, Software, Writing – original draft, Writing – review & editing, Resources, Funding acquisition, Investigation, Supervision. **Alexander L. Yarin:** Writing – review & editing, Resources, Funding acquisition, Investigation, Supervision. **Farzad Mashayek:** Writing – review & editing, Resources, Funding acquisition, Investigation, Supervision.

## Declaration of Competing Interest

The authors declare that they have no known competing financial interests or personal relationships that could have appeared to influence the work reported in this paper.

## Acknowledgments

The authors acknowledge the financial support from the National Science Foundation award CBET-1906497.

## Supplementary materials

Supplementary material associated with this article can be found, in the online version, at doi:10.1016/j.ijmultiphaseflow.2022.103974.

## References


Abels, H., Garcke, H., Grün, G., 2012. Thermodynamically consistent, frame indifferent diffuse interface models for incompressible two-phase flows with different densities. Math. Model. Methods Appl. Sci. 22 https://doi.org/10.1142/S0218202511500138.

Akhlaghi Amiri, H.A., Hamouda, A.A., 2013. Evaluation of level set and phase field methods in modeling two phase flow with viscosity contrast through dual-permeability porous medium. Int. J. Multiph. Flow 52, 22–34. https://doi.org/10.1016/j.ijmultiphaseflow.2012.12.006.

Alpak, F.O., Riviere, B., Frank, F., 2016. A phase-field method for the direct simulation of two-phase flows in pore-scale media using a non-equilibrium wetting boundary condition. Comput. Geosci. 20, 881–908.

Bai, F., He, X., Yang, X., Zhou, R., Wang, C., 2017. Three dimensional phase-field investigation of droplet formation in microfluidic flow focusing devices with experimental validation. Int. J. Multiph. Flow 93, 130–141. https://doi.org/10.1016/j.ijmultiphaseflow.2017.04.008.

Bouwhuis, W., Van Der Veen, R.C.A., Tran, T., Keij, D.L., Winkels, K.G., Peters, I.R., Van Der Meer, D., Sun, C., Snoeijer, J.H., Lohse, D., 2012. Maximal air bubble entrainment at liquid-drop impact. Phys. Rev. Lett. 109, 2–5. https://doi.org/10.1103/PhysRevLett.109.264501.

Caviezel, D., Narayanan, C., Lakehal, D., 2008. Adherence and bouncing of liquid droplets impacting on dry surfaces. Microfluid. Nanofluidics 5, 469–478. https://doi.org/10.1007/s10404-007-0248-2.

Chandra, S., Avedisian, C.T., 1991. On the collision of a droplet with a solid surface. Proc. R. Soc. A Math. Phys. Eng. Sci. 432, 13–41. https://doi.org/10.1098/rspa.1991.0002.

COMSOL®, 2018. CFD Module User 's Guide. COMSOL Multiphysics 1–710.

COMSOL, 2018. COMSOL Multiphysics® v. 5.4 Reference Manual 1622. COMSOL.

Ding, H., Spelt, P.D.M., 2007. Wetting condition in diffuse interface simulations of contact line motion. Phys. Rev. E 75, 1–8. Stat. Nonlinear Soft Matter Phys.

Elmore, P.A., 1990. The entrainment of bubbles by drop impacts. J. Fluid Mech. 220, 539–567. https://doi.org/10.1017/S0022112090003378.

Fink, V., Cai, X., Stroh, A., Bernard, R., Kriegseis, J., Frohnapfel, B., Marschall, H., Wörner, M., 2018. Drop bouncing by micro-grooves. Int. J. Heat Fluid Flow 70, 271–278. https://doi.org/10.1016/j.ijheatfluidflow.2018.02.014.

Ford, R.E., Furmidge, C.G.L., 1967. Impact and spreading of spray drops on foliar surfaces. Soc. Chem. Ind. 25, 417–432.

Hasan, N.O., Prosperetti, A., 1990. Bubble entrainment by the impact of drops on liquid surfaces. J. Fluid Mech. 219, 143–179. https://doi.org/10.1017/S0022112090002890.

Huang, J.J., Shu, C., Feng, J.J., Chew, Y.T., 2012. A phase-field-based hybrid lattice-Boltzmann finite-volume method and its application to simulate droplet motion under electrowetting control. J. Adhes. Sci. Technol. 26, 1825–1851. https://doi.org/10.1163/156856111X599607.

Hung, Y.L., Wang, M.J., Huang, J.W., Lin, S.Y., 2013. A study on the impact velocity and drop size for the occurrence of entrapped air bubbles - water on parafilm. Exp. Therm. Fluid Sci. 48, 102–109. https://doi.org/10.1016/j.expthermflusci.2013.02.013.

Jacqmin, D., 2000. Contact-line dynamics of a diffuse fluid interface. J. Fluid Mech. 402, 57–88.

Jacqmin, D., 1999. Calculation of two-phase navier–stokes flows using phase-field modeling. J. Comput. Phys. 155, 96–127.

Jian, Z., Josserand, C., Popinet, S., Ray, P., Zaleski, S., 2018. Two mechanisms of droplet splashing on a solid substrate. J. Fluid Mech. 835, 1065–1086. https://doi.org/10.1017/jfm.2017.768.

Langley, K.R., Li, E.Q., Vakarelski, I.U., Thoroddsen, S.T., 2018. The air entrapment under a drop impacting on a nano-rough surface. Soft Matter 14, 7586–7596. https://doi.org/10.1039/c8sm01070f.

Levich, V., 1962. Physicochemical Hydrodynamics. Prentice Hall, Upper Saddle River, NJ.

Lim, C.Y., Lam, Y.C., 2014. Phase-field simulation of impingement and spreading of micro-sized droplet on heterogeneous surface. Microfluid. Nanofluidics 17, 131–148. https://doi.org/10.1007/s10404-013-1284-8.

Lin, S., Zhao, B., Zou, S., Guo, J., Wei, Z., Chen, L., 2018. Impact of viscous droplets on different wettable surfaces: Impact phenomena, the maximum spreading factor, spreading time and post-impact oscillation. J. Colloid Interface Sci. 516, 86–97. https://doi.org/10.1016/j.jcis.2017.12.086.

Lowengrub, J., Truskinovsky, L., 1998. Quasi-incompressible Cahn-Hilliard fluids and topological transitions. Proc. R. Soc. A Math. Phys. Eng. Sci. 454, 2617–2654. https://doi.org/10.1098/rspa.1998.0273.

Lyubimova, T., Vorobev, A., Prokopev, S., 2019. Rayleigh-Taylor instability of a miscible interface in a confined domain. Phys. Fluids 31. https://doi.org/10.1063/1.5064547.

Mashayek, F., Ashgriz, N., 1995a. A spine-flux method for simulating free surface flows. J. Comput. Phys. https://doi.org/10.1006/jcph.1995.1222.

Mashayek, F., Ashgriz, N., 1995b. A hybrid finite-element–volume-of-fluid method for simulating free surface flows and interfaces. Int. J. Numer. Methods Fluids 20, 1363–1380. https://doi.org/10.1002/fld.1650201205.

Mehdi-Nejad, V., Mostaghimi, J., Chandra, S., 2003. Air bubble entrapment under an impacting droplet. Phys. Fluids 15, 173–183. https://doi.org/10.1063/1.1527044.

Mitchell, T., Leonardi, C., Fakhari, A., 2018. Development of a three-dimensional phase-field lattice Boltzmann method for the study of immiscible fluids at high density ratios. Int. J. Multiph. Flow 107, 1–15. https://doi.org/10.1016/j.ijmultiphaseflow.2018.05.004.

Moita, A.S., Moreira, A.L.N., 2002. The Deformation of Single Droplets Impacting onto a Flat Surface. SAE Transactions 111, 1477–1489. https://doi.org/10.4271/2002-01-2749.

Pasandideh-Fard, M., Qiao, Y.M., Chandra, S., Mostaghimi, J., 1996. Capillary effects during droplet impact on a solid surface. Phys. Fluids 8, 650–659. https://doi.org/10.1063/1.868850.

Prokopev, S., Vorobev, A., Lyubimova, T., 2019. Phase-field modeling of an immiscible liquid-liquid displacement in a capillary. Phys. Rev. E 99, 1–11. https://doi.org/10.1103/PhysRevE.99.033113.

Pumphrey H.C., Walton A.J. (1988). Sounds produced by water-drop water-surface impacts. Eur. J. Phys. (submitted for publication).

Richard, D., Quéré, D., 2000. Bouncing water drops. Europhys. Lett. 50, 769–775. https://doi.org/10.1209/epl/i2000-00547-6.

Rioboo, R., Marengo, M., Tropea, C., 2002. Time evolution of liquid drop impact onto solid, dry surfaces. Experiments in Fluids 33, 112–124. https://doi.org/10.1007/s00348-002-0431-x.

Sankaran, A., Wu, J., Granda, R., Yurkiv, V., Mashayek, F., Yarin, A.L., 2021. Drop impact onto polarized dielectric surface for controlled coating. Phys. Fluids 33, 062101. https://doi.org/10.1063/5.0054077.

Song, B., Plana, C., Lopez, J.M., Avila, M., 2019. Phase-field simulation of core-annular pipe flow. Int. J. Multiph. Flow 117, 14–24. https://doi.org/10.1016/j.ijmultiphaseflow.2019.04.027.

Tanaka, Y., Washio, Y., Yoshino, M., Hirata, T., 2011. Numerical simulation of dynamic behavior of droplet on solid surface by the two-phase lattice Boltzmann method. Comput. Fluids 40, 68–78. https://doi.org/10.1016/j.compfluid.2010.08.007.

van Dam, D.B., Le Clerc, C., 2004. Experimental study of the impact of an ink-jet printed droplet on a solid substrate. Phys. Fluids 16, 3403–3414. https://doi.org/10.1063/1.1773551.

Vorobev, A., Lyubimova, T., 2019. Vibrational convection in a heterogeneous binary mixture. Part 1. Time-averaged equations. J. Fluid Mech. 870, 543–562. https://doi.org/10.1017/jfm.2019.282.

Vorobev, A., Prokopev, S., Lyubimova, T., 2020. Phase-field modeling of a liquid/liquid immiscible displacement through a network of capillaries. J. Comput. Phys. 421, 109747 https://doi.org/10.1016/j.jcp.2020.109747.

Wang, M.J., Hung, Y.L., Lin, S.Y., 2012. The observation of air bubble entrapment for water droplets impinging on parafilm surface. J. Taiwan Inst. Chem. Eng. 43, 517–524. https://doi.org/10.1016/j.jtice.2012.01.011.

Wang, Y., Gratadeix, A., Do-Quang, M., Amberg, G., 2016. Events and conditions in droplet impact: a phase field prediction. Int. J. Multiph. Flow 87, 54–65. https://doi.org/10.1016/j.ijmultiphaseflow.2016.08.009.

Weiss, D.A., Yarin, A.L., 1999. Single drop impact onto liquid films: neck distortion, jetting, tiny bubble entrainment, and crown formation. J. Fluid Mech. 385, 229–254. https://doi.org/10.1017/s002211209800411x.

Wörner, M., 2012. Numerical modeling of multiphase flows in microfluidics and micro process engineering: a review of methods and applications. Microfluid. Nanofluidics 12, 841–886. https://doi.org/10.1007/s10404-012-0940-8.

Wörner, M., Samkhaniani, N., Cai, X., Wu, Y., Majumdar, A., Marschall, H., Frohnapfel, B., Deutschmann, O., 2021. Spreading and rebound dynamics of sub-millimetre urea-water-solution droplets impinging on substrates of varying wettability. Appl. Math. Model. 95, 53–73. https://doi.org/10.1016/j.apm.2021.01.038.

Wu, Z., Cao, Y., Yao, Y., 2021. Anatomy of air entrapment in drop impact on a solid surface. Int. J. Multiph. Flow 142, 103724. https://doi.org/10.1016/j.ijmultiphaseflow.2021.103724.

Xu, L., Zhang, W.W., Nagel, S.R., 2005. Drop splashing on a dry smooth surface. Phys. Rev. Lett. 94, 1–4. https://doi.org/10.1103/PhysRevLett.94.184505.

Yarin, A.L., 2006. Drop impact dynamics: splashing, spreading, receding, bouncing. Annu. Rev. Fluid Mech. 38, 159–192. https://doi.org/10.1146/annurev.fluid.38.050304.092144.

Yarin, A.L., Roisman, I.V., Tropea, C., 2017. Collision Phenomena in Liquids and Solids. Cambridge University Press, Cambridge. https://doi.org/10.1017/9781316556580.

Yarin, A.L., Weiss, D.A., 1995. Impact of drops on solid surfaces: self-similar capillary waves, and splashing as a new type of kinematic discontinuity. J. Fluid Mech. 283, 141–173. https://doi.org/10.1017/S0022112095002266.

Yarin, A.L., Yazicioglu, A.G., Megaridis, C.M., 2005a. Thermal stimulation of aqueous volumes contained in carbon nanotubes: experiment and modeling. Appl. Phys. Lett. 86, 84–87. https://doi.org/10.1063/1.1844602.

Yarin, A.L., Yazicioglu, A.G., Megaridis, C.M., Rossi, M.P., Gogotsi, Y., 2005b. Theoretical and experimental investigation of aqueous liquids contained in carbon nanotubes. J. Appl. Phys. 97 https://doi.org/10.1063/1.1944214.

Yokoi, K., Vadillo, D., Hinch, J., Hutchings, I., 2009. Numerical studies of the influence of the dynamic contact angle on a droplet impacting on a dry surface. Phys. Fluids 21. https://doi.org/10.1063/1.3158468.

Yue, P., Zhou, C., Feng, J.J., 2007. Spontaneous shrinkage of drops and mass conservation in phase-field simulations. J. Comput. Phys. 223, 1–9. https://doi.org/10.1016/j.jcp.2006.11.020.

Yurkiv, V., Wu, J., Halder, S., Granda, R., Sankaran, A., Yarin, A.L., Mashayek, F., 2021. Water interaction with dielectric surface: a combined ab initio modeling and experimental study. Phys. Fluids 33. https://doi.org/10.1063/5.0046587.

Yurkiv, V., Yarin, A.L., Mashayek, F., 2018. Modeling of droplet impact onto polarized and nonpolarized dielectric surfaces. Langmuir 34, 10169–10180. https://doi.org/10.1021/acs.langmuir.8b01443.

Zhang, Q., Qian, T.Z., Wang, X.P., 2016. Phase field simulation of a droplet impacting a solid surface. Phys. Fluids 28, 022103–022118.